Bull Volcanol (2015) 77:34
DOI 10.1007/s00445-015-0925-z

RESEARCH ARTICLE

Cristobalite in the 2011–2012 Cordón Caulle eruption (Chile)

C. Ian Schipper[1] · Jonathan M. Castro[2] · Hugh Tuffen[3] · Fabian B. Wadsworth[4] · Debra Chappell[5] · Andres E. Pantoja[6] · Mark P. Simpson[5] · Eric C. Le Ru[6]

Received: 10 November 2014 / Accepted: 28 March 2015

Abstract Cristobalite is a low-pressure high-temperature polymorph of SiO_2 found in many volcanic rocks. Its volcanogenic formation has received attention because (1) pure particulate cristobalite can be toxic when inhaled, and its dispersal in volcanic ash is therefore a potential hazard; and (2) its nominal stability field is at temperatures higher than those of magmatic systems, making it an interesting example of metastable crystallization. We present analyses (by XRD, SEM, EPMA, Laser Raman, and synchrotron μ-cT) of representative rhyolitic pyroclasts and of samples from different facies of the compound lava flow from the 2011–2012 eruption of Cordón Caulle (Chile). Cristobalite was not detected in pyroclasts, negating any concern for respiratory hazards, but it makes up 0–23 wt% of lava samples, occurring as prismatic vapour-deposited crystals in vesicles and/or as a groundmass phase in microcrystalline samples. Textures of lava collected near the vent, which best represent those generated in the conduit, indicate that pore isolation promotes vapour deposition of cristobalite. Mass balance shows that the SiO_2 deposited in isolated pore space can have originated from corrosion of the adjacent groundmass. Textures of lava collected downflow were modified during transport in the insulated interior of the flow, where protracted cooling, additional vesiculation events, and shearing overprint original textures. In the most slowly cooled and intensely sheared samples from the core of the flow, nearly all original pore space is lost, and vapour-deposited cristobalite crystals are crushed and incorporated into the groundmass as the vesicles in which they formed collapse by strain and compaction of the surrounding matrix. Holocrystalline lava from the core of the flow achieves high mass concentrations of cristobalite as slow cooling allows extensive microlite crystallization and devitrification to form groundmass cristobalite. Vapour deposition and devitrification act concurrently but semi-independently. Both are promoted by slow cooling, and it is ultimately devitrification that most strongly contributes to total cristobalite content in a given flow facies. Our findings provide a new field context in which to address questions that have arisen from the study of cristobalite in dome eruptions, with insight afforded by the fundamentally different emplacement geometries of flows and domes.

Keywords Cristobalite · Puyehue-Cordón Caulle · Vapour phase crystallization · Rhyolite · Glass corrosion · Devitrification

Editorial responsibility: J.E. Gardner

✉ C. Ian Schipper
schipper.ian@gmail.com

[1] School of Geography, Environment and Earth Sciences, Victoria University of Wellington, PO Box 600, Wellington 6140, New Zealand

[2] Institute of Geosciences, University of Mainz, Becherweg 21, 55099 Mainz, Germany

[3] Lancaster Environment Centre, Lancaster University, Lancaster LA1 4YQ, UK

[4] Department of Earth and Environmental Sciences, Ludwig-Maximilians-Universität München, Theresienstrasse 41, 80333 Munich, Germany

[5] Wairakei Research Centre, GNS Science, 114 Karetoto Road, Taupo 3384, New Zealand

[6] The MacDiarmid Institute for Advanced Materials and Nanotechnology, School of Chemical and Physical Sciences, Victoria University of Wellington, PO Box 600, Wellington 6140, New Zealand

Introduction

Cristobalite is a high-temperature, low-pressure polymorph of crystalline silica (e.g., Heaney 1994). Because pure, particulate cristobalite is toxic when inhaled (Mossman and Glenn 2013), studies on volcanogenic cristobalite have partly been

Published online: 10 April 2015

motivated by a need to determine if it poses a respiratory hazard to communities exposed to fallout of ash from explosive eruptions (Baxter et al. 1999; Horwell and Baxter 2006; Reich et al. 2009; Horwell et al. 2010; Hillman et al. 2012; Horwell et al. 2012), although the actual toxicity of volcanogenic cristobalite is in question (see recent discussion by Damby et al. 2014 and references therein). Regardless of hazards implications, the fact that temperatures in magmatic systems are substantially below the >1,470 °C stability field of pure cristobalite (Deer et al. 1992) makes its formation an interesting example of metastable crystallization in volcanic products (Reich et al. 2009; Horwell et al. 2010, 2013, 2014; Damby 2012; Hillman et al. 2012Damby et al. 2013, 2014). The goals of this study are: (1) to determine the distribution of volcanic cristobalite in different products of the 2011–2012 Cordón Caulle eruption and, once determined, to (2) use textural features of cristobalite-bearing samples to constrain mechanisms and relative rates of its formation during a rhyolite flow-forming eruption.

Pure cristobalite is the stable polymorph of SiO_2 at high *T* and low *P*. At 1 bar, it is bounded by tridymite stability over 867–1,470 °C and melting to silica liquid at 1,727 °C, and it becomes highly unstable at increasing pressure, with β-quartz favoured at P>2–5 bar (see Fig. 1 of Heaney 1994). Despite the small and geologically unfavourable stability field of pure cristobalite, it is a relatively common metastable phase in many types of rocks. This is a result of myriad structural complexities in the SiO_2 system, manifested in phenomena such as: formation of cristobalite directly from quartz (bypassing tridymite) by heating through 1050 °C at 1 bar (Mosesman and Pitzer 1941); persistence of cristobalite from high *T* as rapid quench and the incorporation of impurities inhibit its inversion to quartz (Heaney 1994); or low *T* formation of cristobalite as a diagenetic phase in volcanic and sedimentary rocks (Jones and Segnit 1972). Pure cristobalite is traditionally considered to undergo a transition from its cubic β form to its tetragonal α form with cooling through ~270 °C (Deer et al. 1992), although this transition is complex (Heaney 1994), and has recently been shown to vary from crystal to crystal in natural samples (Damby et al. 2014).

Most studies of volcanic cristobalite have focused on its occurrence in the products of dome eruptions (Swanson et al. 1989; Baxter et al. 1999; Nakada and Motomura 1999; Murphy et al. 2000; Horwell et al. 2003, 2010, 2013, 2014; de Hoog et al. 2005; Pallister et al. 2008; Reich et al. 2009; Damby 2012; Damby et al. 2013), with emphasis on the tendency of domes to collapse and widely disperse ash. In one instance, its formation has been explained by redox reactions in a volcanic plume (Reich et al. 2009); but it is more commonly attributed to deposition from a silica-saturated vapour phase (Baxter et al. 1999; de Hoog et al. 2005; Damby 2012; Horwell et al. 2013) and to devitrification of volcanic glass (Ewart 1971; Swanson et al. 1989; Heaney 1994; Baxter et al. 1999; Damby 2012; Horwell et al. 2013). Because domes form atop the conduits from which they were erupted (Fink and Anderson 2000), the provenance and chemistry of fluids percolating within and through them have been difficult to pinpoint. In their study at Soufrière Hills, Montserrat, Horwell et al. (2013) discuss the probable roles of Cl- and/or F-rich vapours as carriers, referencing experimental work on corrosion and precipitation (de Hoog et al. 2005; Foustoukos and Seyfried 2007). They also introduce concepts of "local" (e.g., derived from the dome itself) versus "bulk" (e.g., fluxed from deeper in the conduit) vapour sources—a distinction we discuss in this work. Damby (2012) recognized that vesicles in some samples with vapour-deposited cristobalite had rinds from which volcanic glass had been corroded, making its constituents available for subsequent transport and deposition (Horwell, personal communication, 2013). Damby (2012) made many key observations regarding the textures of volcanic cristobalite in dome rocks, and his recognition of corrosion rinds as such (see Sections 3.2 and onward) is important to the interpretation of textures presented in this study.

Volcanic cristobalite is also a product of devitrification. Industrial studies have shown cristobalite formation during high-*T* devitrification of aluminosilicate glasses (e.g., Dyson et al. 1997). In rhyolites, spherulites are common cristobalite-bearing features forming near the glass transition (Ewart 1971; Swanson et al. 1989; Castro et al. 2008; Watkins et al. 2009), but non-spherulitic, devitrification-derived cristobalite has also been identified in dome rocks of varying composition (Damby 2012; Horwell et al. 2013) and in the intrusions feeding them (Swanson et al. 1989). Element diffusion rates are temperature dependent, so that extended time at high *T* promotes devitrification (Horwell et al. 2014), and degrees of supercooling control crystallization kinetics (Swanson et al. 1989). This is manifested in the observation that cristobalite content of dome lavas scales inversely with lava extrusion rate (Horwell et al. 2010, 2014; Damby 2012) and is controlled in part by the cooling history of particular parcels of lava (Swanson et al. 1989).

The 2011–2012 eruption of Cordón Caulle, Southern Chile, produced pyroclasts and a laterally extensive compound lava flow, across a full explosive-effusive spectrum (Castro et al. 2013, 2014; Schipper et al. 2013; Tuffen et al. 2013; Bonadonna et al. 2015; Pistolesi et al. 2015). The lava is of particular interest for the investigation of cristobalite because it was transported laterally away from the vent during its emplacement, and unlike a dome is therefore rootless with respect to sustained flux of vapour from the conduit. The sample suite allows us to explore some aspects of volcanic cristobalite formation, framed in reference to the work on volcanic domes by Horwell et al. (2010, 2013, 2014) and Damby (2012), including: (1) its distribution in explosive and effusive eruption products from Cordón Caulle; and (2) the spatial and temporal controls of its formation by different

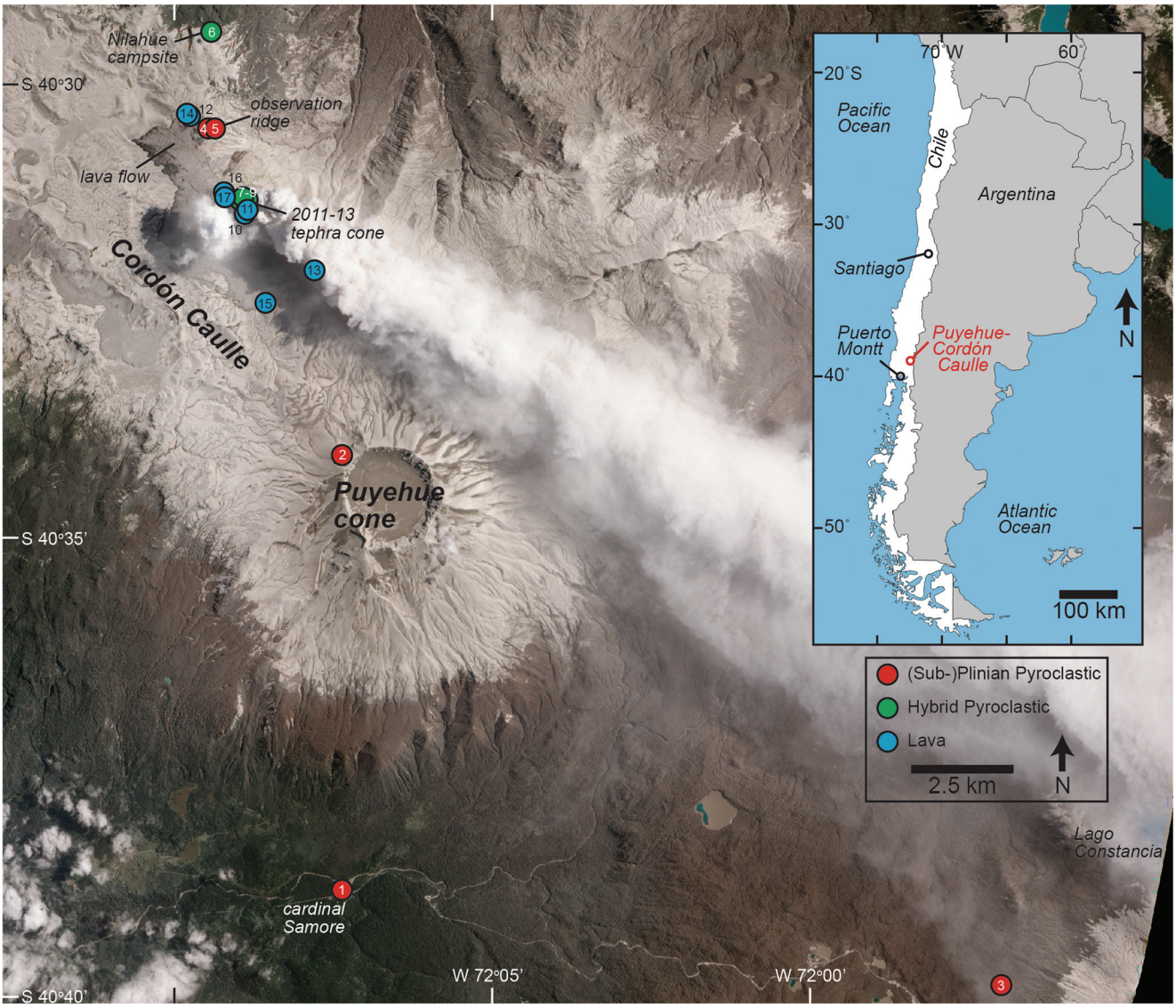

Fig. 1 Sample locations on image of Puyehue-Cordón Caulle volcanic complex taken by the Advanced Land Imager on NASA's Earth Observing-1 (EO-1) satellite on January 26, 2012. *Numbers on location markers* refer to individual samples listed in Table 1. *Inset* shows location of PCC in the Southern Andes, Chile

processes, within different facies of a young rhyolite lava flow.

Puyehue-cordón caulle and the 2011–2012 eruption

The Puyehue-Cordón Caulle volcanic complex, in the Southern Volcanic Zone of the Chilean Andes (Fig. 1) has been active since the Pleistocene (Gerlach et al. 1988; Singer et al. 2008). Activity from the 15 by 4 km massif has been diverse, ranging from effusive outpourings of basalt to Plinian explosions of rhyolite. Prior to 2011, the most recent eruptions had been rhyodacitic, in 1921–1922 and 1960, from the Cordón Caulle fissure system (Lara et al. 2004, 2006).

In 2011, about 2 months of elevated seismicity on Cordón Caulle culminated in the June 4 onset of a Plinian eruption (Silva Parejas et al. 2012; Castro et al. 2013). The eruption column reached a maximum height of 14 km in the first 2 days. This early activity blanketed much of neighbouring Argentina in tephra (Raga et al. 2013) and disrupted air traffic throughout the Southern Hemisphere (Vernier et al. 2013). Within 2 weeks of the eruption onset, effusion of an extensive obsidian lava flow began, and was accompanied by pyroclastic activity for a protracted period lasting until April 2012 (Schipper et al. 2013; Castro et al. 2014). In early 2013, although magma effusion at the vent had ceased months earlier, the obsidian flow continued to advance as lava migration within an insulating crust drove

inflation and flow-front breakouts over 3 km from the vent (Tuffen et al. 2013).

Samples

Samples (Table 1) from the early (sub-) Plinian pyroclastic activity include fine ash (Puy11-Bridge) and lapilli (Puy11-03) that were collected in July 2011 while subplinian activity continued (Puy11-03 is the same used by Castro et al. 2013). Other samples are inferred to be from similar activity because of their distribution far outside of the range limit of pyroclastic deposition that we observed in January 2012 (Fig. 1), when the plume height had diminished to ~2 km (Schipper et al. 2013). The category "hybrid pyroclastic" includes ash (Puy12-Tent; the same used by Schipper et al. 2013) that was collected as it was deposited on fresh surfaces during our observations. Other samples are inferred to be associated with similar activity, by having been collected from the surface of fresh proximal deposits during this period.

The investigated lava samples represent examples of different flow facies, as defined in part by Tuffen et al. (2013) in their investigation of flow emplacement mechanisms. Two "source" samples were obtained from the vent outlet after the eruption ceased (January 2014), from the channel of lava that flowed north to feed the main flow body (P14-L18), and from an adjacent lava body that effused at the outboard edge of the vent (P14-L19) but advanced less than 5 m. A "carapace" block (P14-L03) from the surface of the flow was sampled for its notably isolated vesicles. We include two samples from "breakout" lava lobes, and two from "mature" (or "blocky") lava lobes as defined by Tuffen et al. (2013). Breakouts include one (Puy12-Break) that was advancing at 1.5–3 m/day at the time of sampling in January 2012, and another (Puy13-Lobe01B) that was advancing endogenously in January 2013 (Tuffen et al. 2013). The mature lobes include the rubbly carapace of a lobe that was actively inflating while advancing at 1–1.5 m/day during sampling (Puy12-Block), and one from the dense core of a lobe that had been exposed by lobe collapse (P14-L13m). The core of the main flow channel (P14-L04) was sampled where exposed in a deep crevice on the flow surface.

Analytical methods

Phase abundances were determined using X-ray diffraction (XRD) with a Philips X'Pert Pro instrument at Geological and Nuclear Sciences (GNS) Wairakei. Sample powders were spiked with a known amount of ZnO (10 wt%) as an internal attenuation standard (IAS; Le Blond et al. 2009), and scanned from 2–80° 2θ in steps of 0.010° 2θ and 0.5 s with Co-Kα radiation at 40 kV and 45 mA. Phases were identified using PANalytical X'Pert High Score interpretative software, and their relative abundances quantified using Sietronics' Siroquant software package. For Siroquant calculations, the background was removed (including humps representing amorphous material) as was necessary to avoid large chi-squared values and poor fits as the calculated patterns are free of background. Automatic pre-scaling refinement was then used to obtain an approximate fit, followed by further refinement by adjusting the following Rietveld parameters in order of importance: firstly global refinement (instrumental zero) and then phase refinement (scale, unit cell parameters, halfwidth, preferred orientation). Refinement quality was determined by inspecting the chi-squared, where a measure of goodness fit is between 2 and 5. Conservative errors are approximately ±2 % for phases present at 50–95 % wt%, ±5 % for phases 10–50 % and ±10 % for phases <10 %.

Microtomography (μ-cT) data was collected in Hutch 3B of the Imaging and Medical Beam Line of the Australian Synchrotron, Clayton, Victoria, using their "Ruby" detector with X-ray energy of 45 keV. Scans included 1,800 radiographs with 0.3-s exposure, over 180° rotation. Overlapping vertical scan series were manually stitched together after reconstruction with the X-Tract Imaging Toolbox on the Australian Synchrotron's MASSIVE parallel computing cluster. This yielded large rendered volumes with voxel edge lengths of 13.7 μm/px. Reconstructed image stacks were manipulated and their porosity determined as 3-D volumes and 2-D slice-by-slice batch measurements with ImageJ (Schneider et al. 2012). Volumes were examined and rendered with Drishti (Limaye 2012) open source software package.

Backscatter electron (BSE) imaging on polished sections and secondary electron (SEM) imaging on unpolished rough chips were performed on a JEOL JXA-8230 Superprobe and JEOL 6610 SEM at Victoria University of Wellington, using accelerating voltages of 15 keV and currents of 8.0 nA. Elemental distribution maps in cristobalite-bearing regions were collected using the wavelength dispersive (WDS) element mapping capabilities of the JXA-8230. Element maps were collected with operating conditions of 10–15 keV, 12–20 nA, 1-μm probe diameter, and 400–500-ms dwell times.

Electron microprobe analysis (EPMA) of matrix glasses was performed on the JEOL Superprobe at the University of Mainz, with operating conditions described in Castro et al. (2013). EPMA analysis of cristobalite crystals was performed on the JEOL-8230 at Victoria University, with 15 keV, 12 nA, and 1-μm beam size.

Laser Raman in situ mineral identification was performed on a Horiba JY LabRam HR800 at Victoria University in the backscattering configuration, using a 633-nm He-Ne laser for excitation, a holographic notch filter, a 600 mm^{-1} grating, and a liquid-nitrogen cooled CCD detector. The laser power at the sample was 5 mW. Light was delivered and collected through an Olympus microscope objective of ×100 magnification and

Table 1 Samples

Sample	Description	Collection date	Estimated age[a]	Location	Latitude (S)	Longitude (W)	Elevation	No.
(sub-) plinian pyroclastic samples								
Puy11-Bridge	Fine ash: dry bulk sample collected from ~2-mm-thick deposit on bridge handrail. Mainly pumicious ash, with rare identifiable obsidian chips	3 July 2011	Minutes	Bridge at Cardinal Samore	40°39′42.0″	72°07′40.8″	460	1
Puy12-Pbomb[b]	Pumice bomb: 40-cm white–pinkish pumice bomb with textural gradation from microvesicular rim to oxidized cavity at core	~7 January 2012	Hours	Puyehue Cone Crater Rim	40°34′32.0″	72°07′22.7″	2,050	2
Puy11-03	Pumice lapillus: ~4-cm white pumice lapillus from top of ~20-cm-thick fall sequence	8 July 2011	Minutes	Lago Constancia Trail along dispersal axis	40°40′35.6″	71°57′18.0″	~1,200	3
Puy13-001-IS[b]	Composite bomb: dense obsidian with abundant lithics and flow banding. Original size unknown, collected as chips at edge of a large impact crater on bomb field	6 January 2013	Hours	Observation Ridge Bomb field	40°30′33.6″	72°09′22.5″	1,563	4
Puy13-057-JC[b]	Tube pumice bomb: Whitish, ~30 cm along fabric, ~10 cm perpendicular to fabric	8 January 2013	Hours	Observation Ridge Bomb field	40°30′36.7″	72°09′17.9″	1,527	5
Hybrid pyroclastic samples								
Puy12-Tent	Tube pumice ash: bulk sample of coarse ash dominated by tube pumice<2 mm along fabric, with rare obsidian chips	4 January 2012	minutes	Campsite at Head of Rio Nilahue trail	40°30′29.9″	72°09′20.7″	1,532	6
Puy13-010-IS	Brown pumice bomb: ~40 cm, coarsely vesicular, dark brown pumice bomb	12 January 2013	Hours	Outer rim of 2011–2012 Cordón Caulle tephra cone	40°31′27.5″	72°08′54.1″	1,648	7
Puy13-011-IS	Lg. obsidian bomb: 2.5×1 m, variably breadcrusted. With dense microcrystalline obsidian at rim grading to variably microvesicular interior	12 January 2013	Days	Inner rim of 2011–2012 Cordón Caulle tephra cone	40°31′28.2″	72°08′51.0″	1,645	8
Puy13-013-IS	Sm. obsidian bomb: ~40-cm glassy, non-breadcrusted obsidian bomb	12 January 2013	Days	Inner rim of 2011–2012 Cordón Caulle tephra cone	40°31′28.4″	72°08′50.9″	1,643	9
Lava samples								
P14-L18	Source lava 1: inboard of flow bifurcation at vent. Representative of lava in channel that feeds the entirety of the lava flow	12 January 2014	Days	In vent—at source	40°31′20.9″	72°08′57.3″	1,561	10
P14-L19	Source lava 2: outboard of flow bifurcation in vent. Does not continue to feed main channel of flow.	12 January 2014	Days	In vent—at source	40°31′21.4″	72°08′58.4″	1,566	11
Puy12-Break	Breakout lobe 1: actively advancing breakout from main channel of flow	~11 January 2012	6 months	Adjacent to observation ridge	40°30′27.0″	72°09′41.4″	1,505	12
Puy13-Lobe01B	Breakout lobe 2: actively advancing breakout from long extension of flow to the SE of vent	12 January 2013	18 months	Plateau SE of 2011–2012 vent	40°31′44.1″	72°08′08.6″	1,457	13
Puy12-Block	Mature lobe rubble: blocky lobe directly adjacent to Breakout Lobe 1. Subect to regular gravitational collapses during sampling. Sample is of a collapsed rubble portion of the lobe.	~11 January 2012	3 months	Adjacent to Observation ridge	40°30′28.2″	72°09′39.5″	1,497	14
P14-L13m	Mature lobe core: sample is from intact core of the lobe, below rubbly carapace. Dense, massive.	12 January 2014	32 months	Plateau SE of 2011–2012 vent	40°32′10.6″	72°08′15.9″	1,495	15

Table 1 (continued)

Sample	Description	Collection date	Estimated age[a]	Location	Latitude (S)	Longitude (W)	Elevation	No.
P14-L03	Main channel carapace: rafted block on top of main flow channel. Moderate porosity, with large (~5—10 mm), isolated vesicles	11 January 2014	Days	Exposed on top of main channel of flow.				16
P14-L04	Main channel core: dense core of main channel accessed from top of main channel. Low porosity, with a slate-like fabric	11 January 2014	~32 months	Exposed and accessed from top of main channel of flow.	40°30′59.2″	72°09′04.4″	1,495	17

No. index number used to mark sample locations on Fig. 1

[a] Age is defined as the time from leaving the vent to final emplacement and quenching. Minima are very rough estimates, considered to be short for pyroclastic samples, and correlated with the appearance of a particular lava lobe on various publicly available satellite images. Maxima are from the time of eruption commencement to collection date

[b] These samples inferred to be from early, (sub-)Plinian explosive activity because of their deposition well outside the range of pyroclastic observed during hybrid activity in January 2012

NA 0.9, resulting in a detected area on the sample surface of about 1 μm diameter. The spectral resolution is on the order of 3 cm^{-1}. Confocal imaging was used to eliminate background interference with an observed confocal depth of about 7 μm. Typical spectra were collected using acquisition times of between 10 and 300 s per spectrum.

Detailed analysis of BSE images in ImageJ was used to examine the relationship between groundmass and vapour precipitates. Using Photoshop®, the following were segmented and measured: (1) precipitated crystals protruding from the interiors of vesicle walls; (2) the total area of the corroded regions around vesicles; (3) the microlites in pristine groundmass and in corroded regions. The BSE greyscale range appropriate for segmentation of SiO_2, plagioclase, and glass left heavier phases such as pyroxene and oxides saturated. These are therefore reported collectively as "mafic" crystals.

Results and interpretation

Phase abundances

XRD results (Fig. 2) show amorphous (glass) content to be highest in the Plinian pyroclastic samples, and lowest in the lava samples. This is consistent with the growth of (mainly plagioclase) microlites in portions of the lava that experienced protracted cooling intervals sufficient to overcome nucleation lag effects (e.g., Swanson et al. 1989). In lavas, crystal content and the abundance of all mineral phases increase in the order:

$$\text{Source} < \text{Carapace} < \text{Breakout Lobes} < \text{Mature Lobes} < \text{Core}$$

XRD shows trace quartz (<1 wt%), no tridymite, and widely ranging cristobalite contents (<0.1–23 wt%). No cristobalite was detected in pyroclastic samples of any type. Therefore, an immediate conclusion of this study is that hazards are not of concern, and the following sections consequently deal exclusively with lava samples. Lavas collected at the vent outlet ("source lavas") have only trace (<0.1 wt%) cristobalite, whereas lava from the interior of the main channel ("core lava") contains up to 23 wt%. We note that methods for precisely and efficiently determining SiO_2 polymorph abundances are non-trivial and are continually under development (e.g., Talvitie 1964; Cressey and Schofield 1996; Baxter et al. 1999; Verma et al. 2002; Le Blond et al. 2009); nevertheless, differences in cristobalite abundance are clearly resolved into a robust trend of relative proportions. The silica polymorph abundances in Fig. 2 broadly agree with the abundance of phases observed in thin sections.

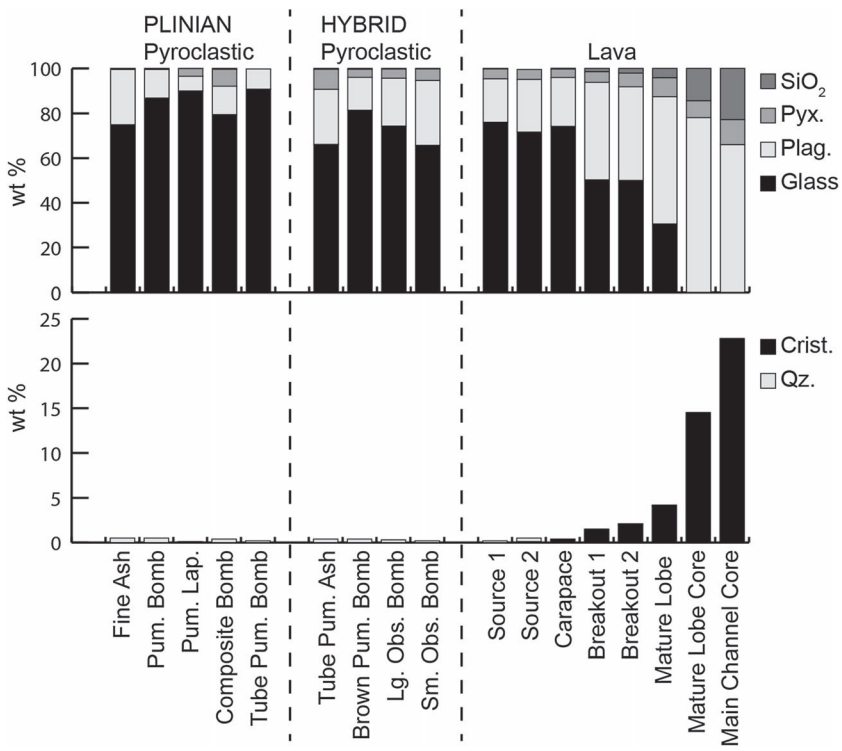

Fig. 2 Cordón Caulle rhyolite mineralogy by XRD. Analyses showing all major phases (upper) and only SiO_2 polymorphs (lower). Errors are approximately ±2 % for phases present at 50–95 % wt%, ±5 % for phases 10–50 % and ±10 % for phases <10 %. All samples have <0.5 wt% quartz (Qz), which is essentially below detection. Note that cristobalite is only present in the lava samples, not in any of the pyroclasts

Lava textures and associated major element distribution

Porosity is highly variable in different facies of the Cordón Caulle lava flow (Fig. 3). Textures in source and carapace samples, which having respectively been emplaced directly at the vent and rafted on top of the flow, are interpreted to have been subject to minimal down-flow modification. Source lavas (Fig. 3a) have contorted vesicles with a high degree of connectivity (and by extension, permeability). Porosity ranges from 21 to 32 % and varies little through the samples. Pore walls are smooth (not corroded as per some instances presented by Damby (2012), see below for further description) and rough chip SEM images show them to be highly vitreous, with the outlines of microlites visible beneath a coating of glass. Carapace lava (Fig. 3b) represents a textural end-member, with only sub-spherical, isolated vesicles totaling 10 % of the volume. Vesicles in carapace lava have corroded rims, identifiable in BSE as regions in which glass has been scavenged from the groundmass leaving only the network of microlites.

Down-flow samples have been subject to textural modification during emplacement that partially or completely overprints original textures. In breakout (Fig. 3c) (and also mature, not shown) lobes, pore space occurs as variably isolated subspherical vesicles, and prolate, contorted, multi-lobed pore networks. Porosity in these samples ranges from 10 to 17 %, but with high slice-by-slice (13.7 μm spacing) variability (e.g. Puy13-Lobe01B porosity ranges from 2 to 36 %). Some of the connected porosity in breakout lava shows no corrosion in BSE/SEM, whereas isolated vesicles in lobe samples have heavily corroded rims. The mature lobe core and main channel core lavas are dense. Some non-collapsed vesicles are still present in the mature lobe core (P14-L13m), where bulk porosity is 2.8 %, but ranges locally up to 17 % in a vesicular band, but nearly all pore space is collapsed in the main channel core sample (P14-L04; Fig. 3d), which has 0.6 % overall porosity that is at all points <4 %. Pore channels in core lava maintain varying degrees of openness, ranging from those that are still ~50 μm wide, to others that are barely discernable in BSE images.

The groundmass of source and carapace lavas have microlites set in a matrix of 50–60 % glass (measured by area on BSE images, slightly lower than abundances determined by XRD; Figs. 3a, b and 4a). Breakout and mature lobe lavas have slightly more crystalline groundmass containing 40–50 % glass with the localized onset of devitrification in occasional crystalline patches (Fig. 4c). These patches of incipient devitrification have an overall spherical shape, but lack the acicular outgrowth from a common nucleus that defines spherulites, and are similar to the "globulites" that precede spherulite formation during devitrification of rhyolitic glass (Lofgren 1971a). The groundmass of the mature lobe core and main channel core lavas (e.g., Fig. 3d) are completely microcrystalline.

Compositional EPMA maps (SiO_2 and K_2O) for several representative textures are shown in Fig. 4. Source lavas show

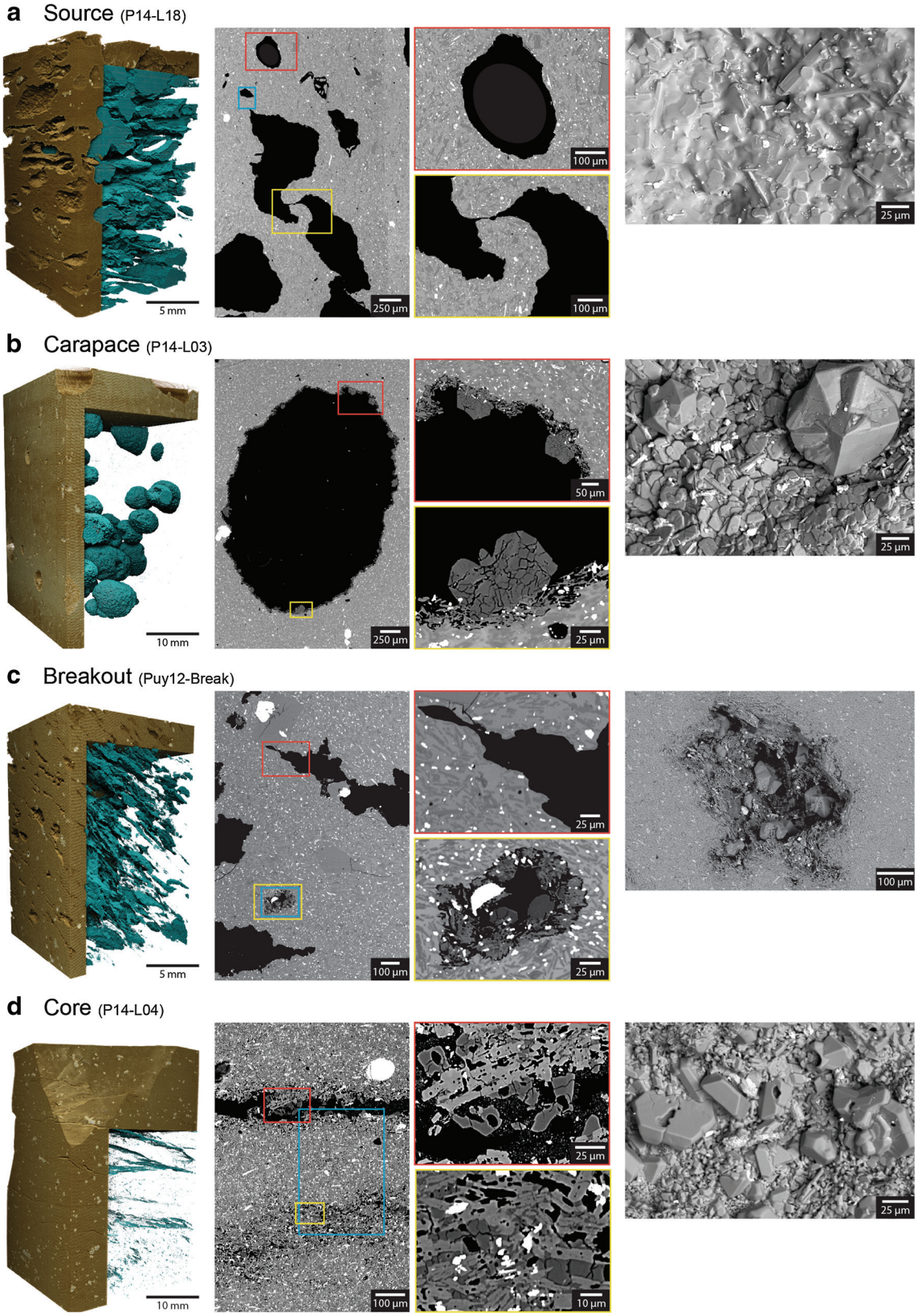

the expected distributions corresponding to microlites set in rhyolitic glass, and their pore space does not contain vapour-deposited crystals (Fig. 4a). Isolated vesicles from breakout lava show high SiO_2 in prismatic cristobalite (described

◀ **Fig. 3** Textures. *Left panels* show μ-cT volume renderings of four lava facies with scales appropriate to show character of porosity. Volume outlines shown with void space transparent, cutaways are inverted, with *solids transparent and voids in blue. Centre panels* show BSE images from the same samples, one overview and two detail panels corresponding to the *red* and *yellow frames*, and *blue frames* marking regions shown as EPMA element maps in Figure 4. *Right panels* show SEM images of unpolished chips from the same samples. **a** Source lava (*P14-L18*) has connected porosity (μ-cT), with non-corroded rims (BSE), and vitreous surfaces (SEM). **b** Carapace lava (*P14-L03*) has isolated porosity (μ-cT) with mildly corroded rims and prismatic cristobalite (BSE). **c** Breakout lava (*PUY12-Break*) has variable porosity (μ-cT), no corrosion in connected pores but extensive corrosion and prismatic cristobalite in isolated pores (BSE/SEM). **d** Core lava (*P14-L04*) has collapsed and sheared pore space (μ-cT) that in some places is nearly completely closed, with broken crystals of cristobalite (BSE/SEM)

below), and K_2O depletion in corrosion rims (Fig. 4b). Comparison to the BSE image shows that the lack of K_2O in the corroded region corresponds to a loss of glass from the matrix, not just loss of alkalis. Element maps of a microcrystalline patch in breakout lava (Fig. 4c) shows <5-μm regions of very high (>90 wt%) SiO_2, and depletion in K_2O. Core lava (Fig. 4d) shows high-SiO_2 in prismatic cristobalite and in abundant patches of >90 wt% SiO_2 ranging from 5 to 25 μm across, distributed throughout the holocrystalline groundmass. The distribution of K_2O in core groundmass is patchy, mostly in channel-like or stellate patterns of depletion, but it is also conspicuously elevated in rare regions within holocrystalline groundmass. Exploratory EPMA analysis showed these to be alkali feldspar (anorthoclase: $Ab_{62}An_6Or_{32}$), which was not previously identified as a groundmass mineral in 2011–2012 Cordón Caulle products (Castro et al. 2013) or in petrographic examination of thin sections prepared for this study, but is in general found along with cristobalite in rhyolitic spherulites (e.g., Ewart 1971).

Cristobalite occurrence and identification

Vapour-deposited cristobalite, ~5–100 μm diameter, in the Cordón Caulle lava is mainly prismatic in habit, with rare platy crystals (Damby 2012; Horwell et al. 2013) protruding from pore walls (Figs. 3b–d, 4b, d, and 6a). Crystals are often twinned, as seen by rough chip SEM (Fig. 3b). In thin section, they show fishscale cracking (Figs. 3b and 6); a diagnostic feature generated by volume contraction during the β–α transition, which occurs ideally at ~270 °C (Deer et al. 1992), but has been experimentally identified to occur closer to ~200 °C in volcanic cristobalite (Damby et al. 2014; Kendrick et al. 2014). Source lavas lack vapour-deposited cristobalite, but in all other lava samples, vapour-deposited crystals are abundant in isolated pore space. In sheared pore channels of core lavas, prismatic cristobalite occurs in irregular, seemingly disrupted, broken, and disaggregated forms (Fig. 3d). Also in core lavas, particles of cristobalite large enough to show fishscale cracking are present in the groundmass, and are not associated with any identifiable open pore space (Fig. 4d, BSE images).

Laser Raman spectroscopy confirms the identity of prismatic cristobalite (Fig. 5). Traverses across the patchy devitrified groundmass of breakout lava and across the holocrystalline groundmass of core lavas indicate that the high-SiO_2 domains (Fig. 4c–d) in these areas are also cristobalite (Fig. 5). Spectra in these regions register a variety of peaks indicative of excitation volumes that include contributions from plagioclase and other groundmass components, but also show the characteristic two peaks of cristobalite at 230 and 417 cm^{-1}.

Chemistry

Representative major element chemistry of groundmass glass from breakout (Puy12-Break; 75.0 wt% SiO_2) and mature lobe rubble (Puy12-Block; 74.9 wt% SiO_2) samples are given in Table 2 (Castro et al. 2013). The average of a suite of EPMA spot analyses (n=68) of prismatic cristobalite that show SiO_2=97.7 wt% and Al_2O_3=2.03 wt%. It has been demonstrated that volcanic cristobalite can structurally incorporate up to 4 wt% Al_2O_3 (Horwell et al. 2003, 2012; Damby 2012; Damby et al. 2013).

Semi-quantitative 2-D image analysis

2-D image analysis permits semi-quantitative comparison between textural components in groundmass and corroded regions of pores, the similarity of which was recognized in dome rocks by Damby (2012). It also permits mass balance calculations to determine if the material deposited as cristobalite could have been sourced adjacent to the same pore in which it is deposited, or whether sourcing from afar is required, as per the discussion of "local" versus "bulk" SiO_2 redistribution by Horwell et al. (2013).

An example of a segmented and false-coloured BSE image of breakout lava is shown in Fig. 6a. The abundance of groundmass microlites (Fig. 6b, measured in area percentage) in breakout (plag, 30–46 %; mafic 4–7 %) and mature lobe lavas (plag, 32–43 %; mafic, 4–8 %) overlap with abundances within corroded rims around pore spaces (breakout plag, 19–47 %; breakout mafic, 5–10 %; mature plag, 39–56 %; mature mafic, 3–8 %). Errors in extrapolating 2-D measurements to 3-D space are specific to the shape and abundance of the targets in question, and are difficult to estimate. Conservatively, relative errors probably fall within ±10 %. The degree of pore infill or occlusion by vapour-deposited cristobalite is similar in isolated pores from breakout (4–27 %) and mature (3–25 %) lobes (e.g., Fig. 6a), suggesting an upper limit to occlusion by vapour deposition. These measurements were made for vesicles that lacked shapes indicative of high shear and/or

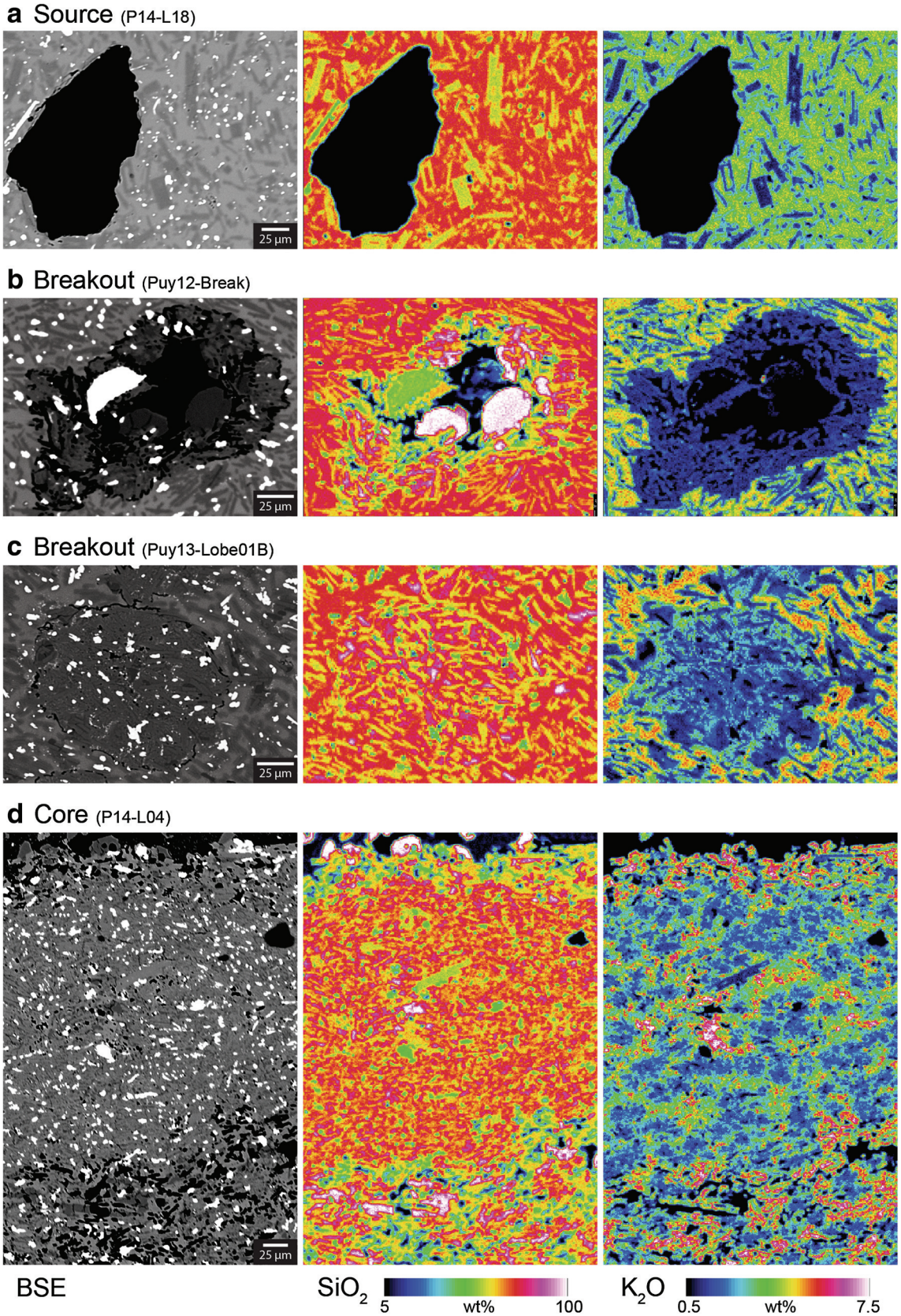

Fig. 4 EPMA element maps of key features. *Left panels* show BSE images of given region; *middle* and *right panels* show SiO_2 and K_2O, respectively. Element distributions are normalized to the same scales from *black to white hot*. Cristobalite shows as *pink–white* (>90 wt%) in SiO_2 maps. Note that all but region c are also shown in Fig. 3

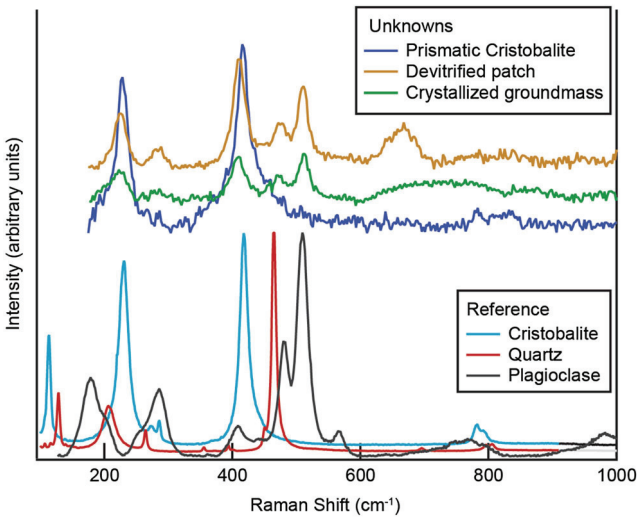

Fig. 5 Phase identification by Laser Raman spectroscopy. Spectra corrected to flat baseline and offset for clarity, with intensities normalized to show relative peak heights. *Bottom* shows reference spectra for cristobalite (Kingma and Hemley 1994), quartz (Gillet and Le Cléac|h 1990), and plagioclase (labradorite; Freeman et al. 2008). *Top* shows representative spectra from prismatic cristobalite in moderately cooled breakout lava (P13-Lobe01B), and from the devitrified region shown in Fig. 4c, and from the crystalline groundmass in slowly cooled core lava (P14-L04; Figs. 3d and 4d). Note that spectra from microcrystalline regions contain contributions from several phases, but that the characteristic two peaks of cristobalite at 230 and 417 cm^{-1} are clear

Table 2 Representative glass and cristobalite chemistry

	Matrix glass[a]		Cristobalite
	Breakout (Puy12-Break)	Mature (Puy12-Block)	
SiO_2	75.0 (0.19)	74.8 (0.92)	97.7 (0.92)
TiO_2	0.52 (0.01)	0.63 (0.08)	0.11 (0.03)
Al_2O_3	11.5 (0.09)	11.2 (0.14)	2.03 (0.83)
FeO^t	2.69 (0.18)	2.66 (0.30)	n.d.
MnO	0.07 (0.02)	0.07 (0.03)	n.d.
MgO	0.13 (0.01)	0.08 (0.01)	n.d.
CaO	0.60 (0.07)	0.47 (0.09)	n.d.
Na_2O	3.64 (0.07)	3.32 (0.08)	0.08 (0.05)
K_2O	4.16 (0.11)	4.9 (0.04)	0.06 (0.05)
P_2O_5	0.05 (0.02)	0.11 (0.03)	n.d.
Cl	0.23 (0.01)	0.31 (0.01)	n.d.
F	0.05 (0.05)	0.09 (0.05)	n.d.
SO_3	0.00 (0.01)	0.01 (0.01)	n.d
Total	98.71 (0.27)	98.78 (0.41)	99.90 (0.16)
n	16	5	68

Compositions are average of n analysis

Total iron as FeO^t

Averages of n analyses, with 1 standard deviation in brackets

n.d. not determined

[a] Compositions from Castro et al. (2013)

collapse (e.g., Fig. 3d), where apparent occlusion would be much greater due to post-vapour deposition loss of pore space.

The mass of oxide *X* either corroded from glass or deposited as cristobalite is denoted m_X, with:

$$m_X = V\rho C_X \quad (1)$$

where $C_X\left(wt\% = \frac{m_{oxide}}{m_{total}}\right)$ is the concentration of each oxide in glass and cristobalite (Table 2). Volumes (V in m^3) are estimated by measuring areas (A in m^2) and assuming unit thickness (1 μm), yielding minima, as $A_{corroded}$ does not capture any pre-existing inter-bubble walls that may have been fully destroyed, and as thin sections do not intersect the maximum radii of vapour-deposited crystals (Higgins 1994). Densities (ρ in kg m^{-3}) of the corroded rhyolite glass and deposited cristobalite are assumed to be equivalent, with $\rho_{glass} \approx \rho_{cristobalite} = 2{,}300$ kg m^{-3} (Deer et al. 1992; Castro et al. 2013). Results of this mass balance for multiple oxides in isolated pores from two lobes (Puy12-Break and Puy12-Block) show the mass of SiO_2 corroded trends toward 1:1 with that deposited as cristobalite (Fig. 6c). This indicates that the SiO_2 deposited as cristobalite could have been scavenged directly from adjacent to the same pore in which it was deposited. Other components, especially alkalis (and those not quantified in cristobalite, not shown), plot below 1:1 marking large discrepancies between the mass corroded and deposited. These are unaccounted for by the deposition of cristobalite, and are discussed in "Lava textures and associated major element distribution" Section.

Discussion

Sample type and cristobalite distribution

Although early reports varied in stating that distal Cordón Caulle ash from the early phases of the eruption did (de Lima et al. 2012) and did not (Caneiro et al. 2011; Wilson et al. 2013) contain cristobalite, we have found no evidence for it in pyroclastic samples from Plinian and sub-plinian phases of activity. The opening of vents at the onset of the 2011–2012 eruption did not disrupt any preexisting rhyolitic flow units from which older cristobalite could have been entrained (Singer et al. 2008) and had low lithic content (Pistolesi et al. 2015). The lack of cristobalite in Plinian ejecta from Cordón Caulle indicates its negligible formation during shallow (2.5–5 km; Castro et al. 2013; Jay et al. 2014) pre-eruptive magma storage and ascent in the conduit.

Pyroclastic material from the period of hybrid activity also lacks cristobalite. Such activity has called into question models of rhyolite volcanism that describe irreversible explosive-to-effusive transitions, showing that lava- and pyroclast-forming magma essentially follow the same

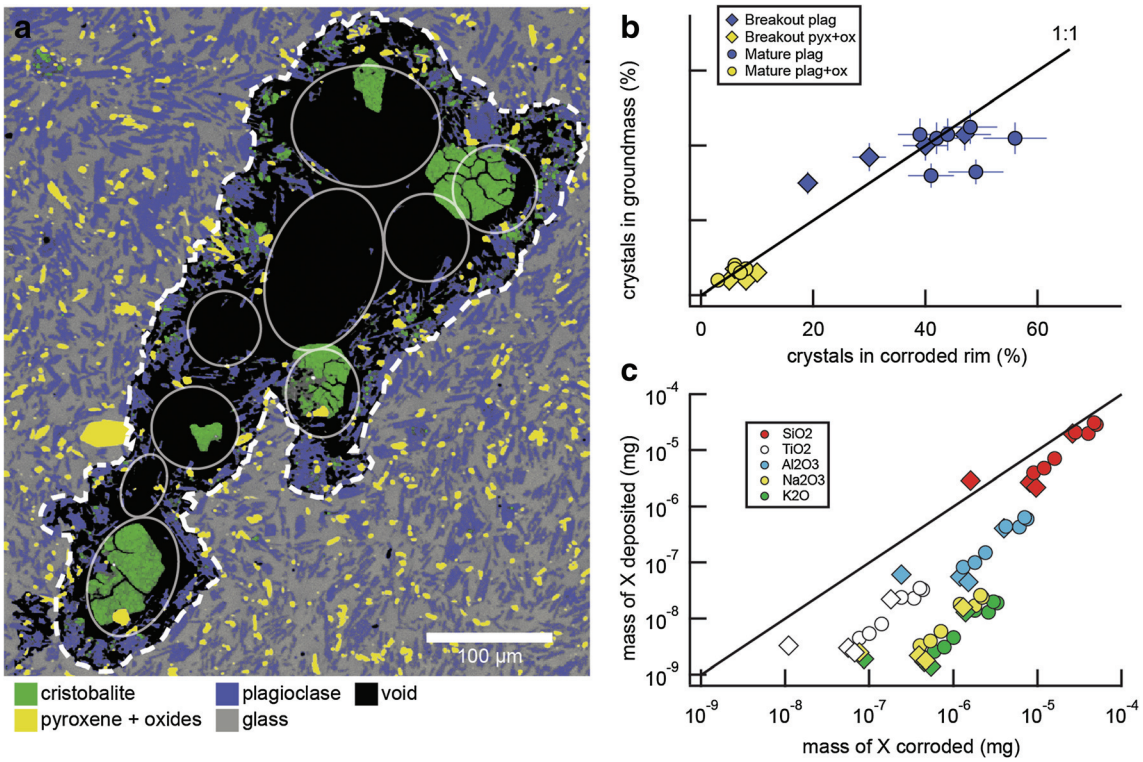

Fig. 6 Image analysis. **a** Example of segmented BSE image (from Puy12-Break), false-coloured in Photoshop® according to different phases. *Dashed white line* marks extent of corrosion, ellipses mark approximations to the pre-corrosion vesicle outlines, in an approach following that of Damby (2012). **b** Microlite content in groundmass and within corroded regions. *Error bars* show estimated ±10 %. **c** Corroded and deposited components. *Data falling below the 1:1 line* indicates components that should have been corroded from the glass, but are not accounted for by their concentrations in the deposited cristobalite. See text for discussion of *errors*

degassing paths (Castro et al. 2014). The implication is that if the efficient conduit outgassing that generated large volumes of degassed lava was accompanied by significant in-conduit corrosion, transport, and deposition of SiO_2, this should have been manifested as cristobalite in both lava and syn-erupted pyroclasts alike. Instead, cristobalite formation must have occurred only within the flow itself.

A positive correlation between dome residence time and cristobalite content has been documented (Damby 2012; Horwell et al. 2014), and studied examples to date have shown it present only in the slowly cooled interior of rhyolitic obsidian domes and their feeding dykes (Swanson et al. 1989). Cordón Caulle pyroclasts and lava from all facies of the flow have the same phenocryst assemblages and abundances (Castro et al. 2013), so that variations in crystallinity recorded by XRD reflect the relative proportion of crystals in the groundmass, and are a proxy for the relative in-flow residence (e.g., cooling) time since degassed lava even at erupted temperatures is firmly in the sub-liquidus field. Three age groups are apparent and are intuitive with the facies of lava they represent: quickly cooled lava (<30 % crystallinity) includes source and carapace lavas that cooled on the order of days; the moderately cooled (50–70 % crystallinity) includes breakout and mature lobes that cooled on the order of several months; and the slowly cooled (fully crystalline) includes core lavas that cooled on the order of years, based simplified calculations of cooling times for the Cordón Caulle lava (Tuffen et al. 2013). This assumes negligible in-conduit cooling, as indicated by overlapping results of Fe–Ti oxide geothermometry in Plinian pumice and lavas (Castro et al. 2013; Militzer 2013). The application of numerical lava flow cooling models (e.g., Patrick et al. 2004) is beyond the scope of the current work, but our results agree with the observation that cristobalite formation is dependent on the length of time spent in the insulated interior of the flow.

Vapour deposition of cristobalite at Cordón Caulle

As per the discussion by Horwell et al. (2013), studies of cristobalite at dome-forming volcanoes (Baxter et al. 1999; Nakada and Motomura 1999; Martel et al. 2000; Murphy et al. 2000; Pallister et al. 2008; Reich et al. 2009; Horwell et al. 2010, 2013; Damby 2012) emphasize the difficulty of differentiating between SiO_2 sourced from directly adjacent to pores in a process of "local redistribution," or from deeper in the volcanic conduit in a process of "bulk transport". Because the Cordón Caulle lava flowed efficiently out of and away from its source (Castro et al. 2013; Schipper et al. 2013; Tuffen et al. 2013), all but the samples taken at the vent outlet

(P14-L18/L19) can be considered "rootless" in terms of volatile flux.

Pore connectivity exerts a strong control on permeability (Mueller et al. 2005), and thus the time available for interfacial contact and reaction between pore walls and percolating fluids. Connected porosity is permeable, potentially over length scales up to those of the entire conduit (Okumura et al. 2009). It therefore limits the contact time of a particular aliquot of vapour, but allows throughput of vapour from farther afield. The converse is true for isolated porosity, which should act as a closed system containing the volcanic gas exsolved from directly adjacent melt. At Cordón Caulle, the source and carapace lava samples (Figs. 3a–b) are both rapidly cooled, and are both interpreted to have pore structures representative of those that developed in the conduit (e.g., without down-flow modification). However, their pores are variably connected (source) and isolated (carapace), demonstrating that shear localization (Wright and Weinberg 2009) within the conduit yields lava with heterogeneous textures even from first emergence at the surface. The key observation in these samples is that connected pores of source lavas lack corrosion and vapour-deposited cristobalite (Figs. 3a and 4a), whereas isolated pores of carapace lava have them (Figs. 3b). The inference is that for these similarly and rapidly cooled lava samples, vapour corrosion and deposition only occurred in pores that were isolated and impermeable to vapour percolation and outgassing.

The source and carapace end members are illustrative of the textural variability at the vent outlet, but textures in most of the flow are modified during transport away from the vent. Porosity that may have been isolated at the time of cristobalite formation does not necessarily remain isolated ad infinitum, and processes superimposed on original textures must be taken into account when considering preserved textures. Tuffen et al. (2013) showed that a key lava emplacement mechanism at Cordón Caulle involved internal, endogenous flow beneath a thermally insulating carapace, which includes both: (1) inflation resulting from degassing-induced nucleation of new pore space and/or expansion of existing pores; and (2) horizontal flow that is accompanied by shear coalescence, outgassing, and compaction. Three-dimensional analysis of the Cordón Caulle lobes showed vertical and horizontal movement to be spatially heterogeneous, but with vertical velocities consistently subordinate to horizontal velocities of a given lobe (Tuffen et al. 2013). Cordón Caulle lava samples in turn show different degrees of modification depending on the flow facies from which they were collected, evolving with extended high-temperature residence within the flow to lower overall porosity and more intensively sheared, compacted pore geometries. Moderately cooled samples from advancing lobes have intermediate textures with both connected and isolated pores. The isolated populations in these flow lobes likely include some vesicles that were newly formed in lobe inflation events and others that were preserved from the vent outlet by strain localization that tends to concentrate deformation into previously strained regions of bubble-bearing melt (Okumura et al. 2008; Wright and Weinberg 2009). Similarly, the connected pore networks in flow lobes represent some networks that were made to coalesce by shear, and others that were continuously connected for their entire post-vent lifetimes. Although some complexity is introduced by having a flow history superimposed on the textures, it remains that wall textures (e.g., ±corroded) of pores in lobe samples are not dissimilar to those of the in rapidly cooled lavas: isolated pores being ubiquitously corroded and some connected pores maintaining vitreous walls (Fig. 3c). Slowly cooled lava from the core of the flow represents a texturally evolved end member, with completely modified pore structures (Fig. 3d). Porosity is rare and in connected channels bears extensive evidence for corrosion and cristobalite vapour deposition. Although these channels must be classified as (at least linearly) "connected porosity" in their preserved state, their structure cannot be taken as representative of pore structure at the time of vapour-driven surface processes.

Prismatic cristobalite in isolated pores (Fig. 3b, c) of most lava samples are pristine (euhedral), whereas those in compacted pore channels of core lavas appear disaggregated and broken, with crystal particles seemingly toppled and redistributed (Fig. 3d, BSE/SEM images). We attribute this to breakage and cleaving of prismatic cristobalite as pores close by compaction and shear around them. On a lava scale, this may be due to the application of greater shear stresses in the core than in the upper parts of the flow, simply due to a greater thickness of lava overburden (tens of metres) applied to the core lava interior. Pervasive fishscale cracking in cristobalite may make it subject to disaggregation along the network of tensile cracks (Horwell et al. 2013). Complete closure of pore channels then sees the incorporation of broken crystals into the densifying lava, so that while they once protruded into void space, they are eventually enclosed in a melt-microlite matrix. Evidence for this can be seen in core lava, at the site of outsized cristobalite in the groundmass (large SiO_2-rich region in Fig. 4d). This example is not only ~10–20 times larger than surrounding groundmass cristobalite, it also still retains fishscale cracking that is otherwise observed only in vapour-deposited crystals of the Cordón Caulle lava, not in typical groundmass cristobalite.

Errors in image analysis notwithstanding, the close match of crystal populations in corrosion rims and adjacent groundmass (Fig. 6b) implies that the only significant difference between the corroded regions and the original pristine groundmass is loss of glass from the matrix. This is consistent with observations of Damby (2012), and is a characteristic he used to identify the origin and significance of corrosion rims. In our Cordón Caulle samples, the mass balance calculations (Fig. 6c) indicate that the SiO_2 deposited as cristobalite in a

given pore is close to 1:1 against the SiO_2 corroded from adjacent to the same pore, with the amount deposited always less than that corroded. This suggests that SiO_2 was corroded and deposited locally, lending support to the "local SiO_2 redistribution" model discussed by Horwell et al. (2013). We have not provided error bars in Fig. 6c because they are not reliably quantifiable. Offset to lower SiO_2 is partly an artifact, because the shape of prismatic cristobalite (roughly approximating spheres protruding from vesicle walls) will systematically be underrepresented in cut planes of thin sections. Although this precludes strict adherence to 1:1, the trend is for proportionally increasing corroded/deposited SiO_2 in a given pore.

Data for Al_2O_3 is scattered (Fig. 6c) and other elements stripped from corroded regions (Fig. 4b) are largely unaccounted for by the deposited cristobalite. No observation in this study can identify a sink for these elements. Horwell et al. (2013) surmised that missing volatilized elements could have been transported to surface fumaroles in passing vapours. Their suggestion is in keeping with early studies in which volcanologists formed sublimates in silica tubes that were inserted directly into fumaroles of volcanic domes (Le Guern and Bernard 1982; Bernard and Le Guern 1986). Such in situ sampling showed a strong along-tube temperature dependence on the minerals deposited, the hottest zone being cristobalite-rich (from 900 °C through to ~570 °C), successive zones being rich in various metal and sulfur compounds, and followed by NaCl and KCl as major components at low temperature. Such percolation of vapours in the context of the Cordón Caulle lava flow would require that pore networks were connected and discharging vapour to the surface. For the case of pores that were connected from the vent outlet, direct discharge of vapour would have precluded corrosion. Further downflow, passage of vapours could have occurred if isolated pores became connected by shear and/or corrosion of inter-pore walls (as seen in Fig. 6) in a limited temperature interval after high-*T* deposition of cristobalite and before lower-*T* deposition of other components (Le Guern and Bernard 1982). However, although conceptually plausible, this admittedly would require a highly specific set of circumstances and sequence of events. Nonetheless, a relevant macroscopic observation is that there is strong surface discoloration by vapour-phase precipitate minerals conspicuously formed at the source region of Cordón Caulle lava breakouts (Tuffen et al. 2013), consistent with vapour transport through interconnected lava porosity and precipitation at lower-temperature conditions at the surface.

An alternative explanation for the missing elements is that crystalline silica has relatively high preservation potential compared to any of a host of volcanogenic sublimates or salts (Rosenberg 1988; Delmelle et al. 2007) that might also have been produced, and that it should be far more abundant than any other phase because of SiO_2 being the main constituent of rhyolite glass. Although these "should" still be present in pores that remained isolated, many volcanic sublimates are ephemeral, and many are released rapidly upon encountering water (e.g., Jones and Gislason 2008). Also, components such as K_2O are actually relatively minor constituents of the corroded glass (Table 2). Thus, within the closed system of a given pore, the volume of any non-SiO_2 sublimate deposited in pore space would be miniscule. Provided such compounds survived collection and preparation, they would still be difficult to detect without surface-sensitive techniques such as X-ray photoelectron spectroscopy or atomic force microscopy—these having been used by Delmelle et al. (2007) to examine compounds and textures generated by acid dissolution on volcanic ash, which exist only at the nanometer scale. The fate of some corroded elements remains an outstanding question, requiring approaches that specifically target the compounds that may be present in trace amounts and have poor preservation potential.

The chemical durability of glasses at low temperatures has been studied extensively (e.g., Clark and Yen-Bower 1980; Hench et al. 1980; Adams 1984; Bunker 1994; Hamilton and Pantano 1997; Oelkers 2001; Icenhower et al. 2004; Cailleteau et al. 2008; Declercq et al. 2013), but studies at magmatic temperatures are lacking. Glass corrosion can proceed by etching or leaching - depending on the type of attacking solution (Adams 1984; Bunker 1994; Icenhower et al. 2004; Cailleteau et al. 2008). Etching involves the direct breakdown of the silica network by alkaline solutions. Leaching involves the initial scavenging of alkalis from the glass by an acid, which may or may not be followed by Si framework breakdown depending on the effectiveness of surface gel formation, which can slow continued degradation of the structural network (Oelkers 2001; Icenhower et al. 2004). In the Cordón Caulle lavas, glass has been physically corroded from around pores (Figs. 3b–c, 4b, and 6). The precise nature of the corroding fluid is not explicitly known, but is inferred to have been predominantly magmatic H_2O that exsolved to form isolated vesicles, with minor but important concentrations of the acidifying complexes S (0.01 wt% of lava matrix glass; Table 2), Cl (0.32 wt% residual), and F (not determined) that typify volcanic gases, noting that Cl and F are both known contributors to SiO_2 redistribution potential (de Hoog et al. 2005; Shmulovich et al. 2006; Foustoukos and Seyfried 2007). We note several complexities to pinpointing a corroding/depositing vapour: (1) magmatic gases are dominated by H_2O, and thus can only form dilute solutions with limited SiO_2-carrying capacity (de Hoog et al. 2005); (2) vapour likely oscillates about Si-saturation, corroding and depositing at rates that vary with chemical activity and time (Horwell et al. 2013); (3) the wide temperature interval through which lava cools results in drastic temporal changes to corrosion rates, vapour reactivity, and deposition kinetics (Declercq et al. 2013); (4) magmatic fluids are both alkali-rich and

acidic, driving corrosion that likely includes cooperative components of etching and leaching; (5) the specific acidic complexes present in the corroding vapour can enhance glass corrosion, i.e., pH alone is not the only factor in determining corrosion rates (Wolff-Boenisch et al. 2004a); (6) most experimentation has been done with pure glass powders, not coherent glass surfaces (bubble walls) containing crystalline phases that corrode at different rates (Icenhower et al. 2004); and (7) the vapour in a flow will be heterogeneous in the sense that isolated pores formed in the conduit should contain gases exsolved at higher pressure than those in isolated pores generated during inflation events of a flow lobe.

These complexities preclude an absolute calculation of corrosion rates in the Cordón Caulle lava, as even more importantly does the lack of corrosion rate data at magmatic and/or cristobalite sublimation (>570 °C; Bernard and Le Guern 1986) temperatures; however, we can illustrate the differential timescales of corrosion by drawing on the observation that glass is lost, but plagioclase remains, in corroded regions (Fig. 6). Dissolution rates (R_X in mole per square meter per second) are expressed as a series of curves in Figure 7, as the time (t) to corrode to a certain depth (d) from the original pore surface:

$$t = \frac{d}{V_X R_X} \tag{2}$$

where V_X is molar mass, $V_{plag}=1.04\times10^{-4}$ m^3 mol^{-1} (Lange and Carmichael 1990) and $V_{glass}=2.62\times10^{-5}$ m^3 mol^{-1}, the latter calculated using the composition given in Table 2 at 25 °C and 1 atm (Lange and Carmichael 1990).

Comparison of dissolution rates (R_X in mol m^{-2} s^{-1}) in acidic solutions from two studies where experimental conditions match (T=25 °C and pH=4.0) shows that rhyolite with 70.2 wt% SiO_2 dissolves at $\log_{10}(R_{glass})=-9.69$ mol m^{-2} s^{-1} (Wolff-Boenisch et al. 2004b), and plagioclase dissolves at $\log_{10}(R_{plag})=-11.1$ mol m^{-2} s^{-1} (Oxburgh et al. 1994). Plagioclase dissolution rates are dependent on mineral composition (Casey et al. 1991), this rate being for compositions similar to Cordón Caulle andesine (An37; Castro et al. 2013). For fixed T and pH, an acidic corrosion front in rhyolite glass will advance ~1–1.5 orders of magnitude more quickly than in plagioclase (Fig. 7). Data for corrosion rates at elevated temperature are limited, however experiments by Declercq et al. (2013) are useful for assessing the influence of different fluid parameters (T, pH; but without specifying the type of acid). Rates of glass corrosion are more strongly influenced by T than pH.

Figure 7 also shows corroded rim depths in Cordón Caulle lavas. Using total crystallinity (Fig. 2) as a proxy for cooling time in each lava sample, the corrosion depths roughly follow similar trends to corrosion timescales at any fixed T and pH, suggesting that it is appropriate to treat the volcanic corrosion problem this way; however, that the absolute times associated with the crystallization and corrosion are far from sufficiently constrained to be yield absolute times. It is certain that at higher temperatures, such as those of the Cordón Caulle at vent exit, corrosion rates would have been orders of magnitude faster than those shown in Fig. 7.

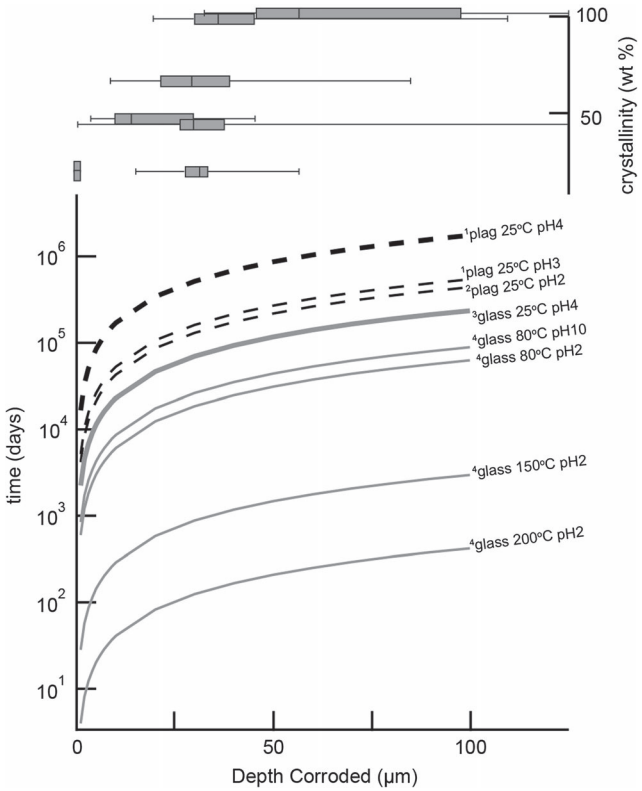

Fig. 7 Corrosion timescales expressed as depth of corrosion from original solid–vapour interface. Measured corrosion rim thicknesses shown as *box* and *whisker plots*, plotted against total crystallinity (by XRD) as a proxy for residence time in the flow; absolute residence times are not accurately known. Curves for corrosion of rhyolite glass and plagioclase by solutions varying in T and pH, plotted against time. Note that for fixed T and pH (*heavy curves*), glass is etched ~1.5 orders of magnitude faster than plagioclase. Sequence of curves for glass demonstrates a stronger dependence on T than pH. Note that lava actually cooled through much higher temperatures than covered by the corrosion rates shown, and the timescales shown are extreme minima. *1* Oxburgh et al. (1991); *2* Casey et al. (1994); *3* Wolff-Boenisch et al. (1991); *4* Declercq et al. (2004b)

Groundmass crystallization and devitrification

The most cristobalite-rich samples are those that cooled slowly and have holocrystalline groundmass. Laser Raman analyses indicate cristobalite as a groundmass component (Fig. 5; also noted by Horwell et al. 2013), concurring with previous studies that attribute its formation to devitrification (Swanson et al. 1989; Baxter et al. 1999; Damby 2012; Horwell et al. 2013, 2014). Devitrification is generally considered to be a process occurring at or below the glass transition (T_g), where

slow cooling offsets temperature-limited diffusion of crystal-forming elements in the interior of the flow, at undercoolings that vary with local intrinsic (composition, H_2O content) and extrinsic (T, P) properties (Swanson et al. 1989). When discussing if spherulites grow in rhyolite below T_g, Watkins et al. (2009) noted that across T_g there is no change in diffusion mechanism (e.g., no inflection in diffusivity versus temperature; see their Fig. 9). They thus concluded that T_g was not in itself a definitive barrier to crystallization. Following this logic, the process of groundmass cristobalite formation should be the same above and below T_g, blurring the distinction between what should be considered crystallization and what should be considered devitrification. It is generally accepted from studies on crystallization regimes in obsidian that order follows: phenocrysts–microlites–devitrification; each occurring under different conditions during the lifetime of a cooling lava (Swanson et al. 1989). Groundmass cristobalite at Cordón Caulle likely began forming only after microlite crystallization had fractionated residual melt into a fully polymerized state (at ~77 wt% SiO_2; Zhang 2008) as it has been noted that although fully polymerized rhyolite melt lacks long-range order, it has short-range order with structure more similar to that of cristobalite than quartz (Mysen and Richet 2005), the heterogeneity of this short-range order manifesting as spatial variability in devitrification textures (Lofgren 1971b). Quantification of the cooling interval/rate in which groundmass cristobalite forms at Cordón Caulle requires targeted petrological experiments.

As noted earlier, samples without groundmass cristobalite often have vapour-deposited cristobalite (Fig. 3b), suggesting that these processes act independently (Damby 2012). It provides circumstantial evidence that the presence of cristobalite nuclei may not be a necessary precondition to its subsequent deposition from a vapour (Renders et al. 1995), and that under favourable conditions, vapour deposition occurs earlier in flow evolution than devitrification. It has also been noted that alkali-rich solutions such as those that would have been generated during glass corrosion can significantly increase rates of rhyolite devitrification (Lofgren 1970). It therefore would be a synthetic division to completely divorce vapour reaction from devitrification, especially given that during protracted cooling intervals these probably occur simultaneously.

Conclusions

Cristobalite distribution in the 2011–2012 Cordón Caulle eruption products demonstrates that there are no imminent respiratory hazards associated with pyroclastic phases of the eruption, and provides a new field perspective on questions of volcanic cristobalite formation that have arisen from studies of silicic dome eruptions.

Firstly, Cordón Caulle samples provide evidence in support of the "local SiO_2 redistribution" origin of vapour-phase cristobalite discussed by Horwell et al. (2013):

(1) Cristobalite is absent from pyroclasts but present in lava, despite both having had the same in-conduit degassing history.
(2) The Cordón Caulle flow is rootless with respect to flux of conduit-derived fluids, yet contains vapour-deposited cristobalite.
(3) Vapour corrosion and deposition is ubiquitous in isolated vesicles but rare in connected pore networks.
(4) Deposited SiO_2 in a given pore can have been corroded from adjacent to the same pore.

Secondly, Cordón Caulle samples also allow a qualitative evaluation of the relative roles of vapour deposition and groundmass devitrification in generating cristobalite in rhyolite lava flows:

(1) Samples that contain vapour-deposited cristobalite may or may not contain devitrification products, suggesting that vapour deposition and devitrification act independently, but may act concurrently
(2) The highest concentrations of cristobalite contents are achieved only when groundmass crystallization and devitrification is extensive, in the most slowly cooled samples from thermally insulated flow interiors.

In these, the processes governing groundmass cristobalite formation in rhyolite lava flows are similar to those in dome rocks of varying composition (Damby 2012).

The Cordón Caulle lava flow additionally yields new information regarding the importance of pore connectivity on the reaction of corroding/depositing vapour and gives evidence for redistribution of previously formed cristobalite during in-flow evolution of pore space. It also shows that devitrification following groundmass crystallization is the most effective process for generating high cristobalite abundance in a cooling rhyolite lava flow. This work also highlights several other areas that require further investigation, which include investigation of the sinks for minor components corroded from volcanic glass, and refinement of the T–P space under which vapour reaction and devitrification processes are most effective.

Acknowledgments CIS acknowledges support from the ERC grant 202844 awarded to A. Burgisser under the EU FP7, from Victoria University FSRG grant number 205424, and from the Royal Society of New Zealand Cook Fellowship awarded to C.J.N. Wilson. JMC was supported by the VAMOS research center at the University of Mainz. HT acknowledges support from a Royal Society University Research Fellowship. FBW acknowledges support from the EU FP7 grant 282759 (VUELCO). Access to the Australian Synchrotron's IMBL was granted under

proposals 2013/2-M7045 and 2014/1-M7574, with travel support from the New Zealand Synchrotron Group Ltd., and assistance from M. Edwards, J. Cowlyn, and B.M. Kennedy of the University of Canterbury.

References

Adams PB (1984) Glass corrosion. J Non-Cryst Solids 67:193–205

Baxter PJ, Bonadonna C, Dupree R, Hards VL, Kohn SC, Murphy MD, Nichols A, Nicholson RA, Norton GE, Searl A, Sparks RSJ, Vickers BP (1999) Cristobalite in volcanic ash of the Soufriere Hills Volcano, Montserrat, British West Indies. Science 283:1142–1145

Bernard A, Le Guern F (1986) Condensation of volatile elements in high-temperature gases of Mount St. Helens. J Volcanol Geotherm Res 28:91–105

Bonadonna C, Cioni R, Pistolesi M, Elissondo M, Baumann V (2015) Sedimentation of long-lasting wind-affected volcanic plumes: the example of the 2011 rhyolitic Cordón Caulle eruption, Chile. Bull Volcanol 77:13. doi:10.1007/s00445-015-0900-8

Bunker BC (1994) Molecular mechanisms for corrosion of silica and silicate glasses. J Non-Cryst Solids 179:300–308

Cailleteau C, Angeli F, Devreux F, Gin S, Jestin J, Jollivet P, Spalla O (2008) Insight into silicate-glass corrosion mechanisms. Nat Mater 7:978–983. doi:10.1038/nmat2301

Caneiro A, Mogni L, Serquis A, Cotaro C, Wilberger D, Ayala C, Daga R, Poire D, Scerbo E (2011) Análisis de cenizas volcánicas Cordón Caulle (Complejo Volcanico Puyehue-Cordón Caulle) Erupción 4 de Junio de 2011. Informe Cenizas Volcánicas - CNEA:1-17

Casey WH, Westrich HR, Holdren GR (1991) Dissolution rates of plagioclase at pH = 2 and 3. Am Mineral 76:211–217

Castro JM, Beck P, Tuffen H, Nichols ARL, Dingwell DB, Martin MC (2008) Timescales of spherulite crystallization in obsidian inferred from water concentration profiles. Am Mineral 93:1816–1822

Castro JM, Schipper CI, Amigo A, Silva Parejas C, Mueller S, Jacob D, Militzer AS (2013) Storage and eruption of near-liquidus rhyolite magma at Cordón Caulle, Chile. Bull Volcanol 75:702. doi:10.1007/s00445-013-0702-9

Castro JM, Bindeman IN, Tuffen H, Schipper CI (2014) Explosive origin of silicic lava: Textural and δD-H2O evidence for pyroclastic degassing during rhyolite effusion. Earth Planet Sci Lett 405:52–61. doi:10.1016/j.epsl.2014.08.012

Clark DE, Yen-Bower EL (1980) Corrosion of glass surfaces. Surf Sci 100:53–70

Cressey G, Schofield PF (1996) Rapid whole-pattern profile-stripping method for the quantification of multiphase samples. Powder Diffract 11:35–39

Damby DE (2012) From dome to disease: The respiratory toxicity of volcanic cristobalite. PhD thesis. Durham University, Durham, p 359. http://etheses.dur.ac.uk/7328/

Damby DE, Horwell CJ, Llewellin EW, Nattrass C (2013) Cristobalite in volcanic domes: crystallization of a meta-stable mineral. In: IAVCEI 2013 Scientific Assembly. Kagoshima, Japan

Damby DE, Llewellin EW, Horwell CJ, Williamson BJ, Najorka J, Cressey G, Carpenter M (2014) The α-β phase transition in volcanic cristobalite. J Appl Cristallogr 47:1205–1215. doi:10.1107/S160057671401070X

de Hoog JCM, van Bergen MJ, Jacobs MHG (2005) Vapour-phase crystallisation of silica from SiF4-bearing volcanic gases. Ann Geophys 48:775–785

de Lima EF, Sommer CA, Cordeiro Silva IM, Netta AP, Lindenberg M, Marques Alves RC (2012) Morfologia e química de cenizas do vulcão Puyehue depositadas na região metropolitana de Porto Alegre em junho de 2011. Revista Brasiliera de Geociencias 42:265–280. doi:10.5327/Z0375-75362012000200004

Declercq J, Diedrich T, Perrot M, Gislason SR, Oelkers EH (2013) Experimental determination of rhyolitic glass dissolution rates at 40–200 °C and 2 < pH < 10.1. Geochim Cosmochim Acta 100:251–263. doi:10.1016/j.gca.2012.10.006

Deer WA, Howie RA, Zussman J (1992) An Introduction to the Rock-Forming MInerals 2nd Edition. John Wiley and Sons, New York

Delmelle P, Lambert M, Dufrêne Y, Gerin P, Óskarsson (2007) Gas/aerosol-ash interaction in volcanic plumes: New insights from surface analyses of fine ash particles. Earth Planet Sci Lett 259:159–170. doi:10.1016/j.epsl.2007.04.052

Dyson DJ, Butler MA, Hughes RJ, Fisher R, Hicks GW (1997) The devitrification of alumino-silicate ceramic fibre materials - The kinetics of the formation of different crystalline phases. Ann Occup Hyg 41:561–590

Ewart A (1971) Chemical changes accompanying spherulitic crystallization in rhyolitic lavas, Central Volcanic Region, New Zealand. Mineral Mag 38:424–434

Fink JH, Anderson SW (2000) Lava Domes and Coulees. In: Sigurdsson H, Houghton B, McNutt SR, Rymer H, Stix J (eds) Encyclopedia of Volcanoes. Academic Press, New York, pp 307–319

Foustoukos DI, Seyfried WE Jr (2007) Quartz solubility in the two-phase and critical region of the NaCl-KCl-H2O system: Implications for submarine hydrothermal vent systems at 9o50' N East Pacific Rise. Geochim Cosmochim Acta 71:186–201. doi:10.1016/j.gca.2006.08.038

Freeman JJ, Wang A, Kuebler KE, Jolliff BL, Haskin LA (2008) Characterization of natural feldspars by raman spectroscopy for future planetary exploration. Can Mineral 46:1477–1500. doi:10.3749/canmin.46.6.1477

Gerlach DC, Frey FA, Moreno-Roa H, Lopez-Escobar L (1988) Recent volcanism in the Puyehue-Cordón Caulle region, southern Andes, Chile (40.5o S): Petrogenesis of evolved lavas. J Petrol 29:333–382

Gillet P, Le Cléac'h A (1990) High-temperature raman spectroscopy of SiO_2 and GeO_2 polymorphs: Anharmonicity and thermodynamic properties at high-temperatures. J Geophys Res 95(B13):21635–21655. doi:10.1029/JB095iB13p21635

Hamilton JP, Pantano CG (1997) Effects of glass structure on the corrosion behavior of sodium-aluminosilicate glasses. J Non-Cryst Solids 222:167–174

Heaney PJ (1994) Structure and chemistry of the low-pressure silica polymorphs. Rev Mineral 29:1–40

Hench LL, Clark DE, Yen-Bower EL (1980) Corrosion of glasses and glass-ceramics. Nucl Chem Waste Manag 1:59–75

Higgins MD (1994) Numerical modeling of crystal shapes in thin sections: Estimation of crystal habit and true size. Am Mineral 79:113–119

Hillman SE, Horwell CJ, Densmore AL, Damby DE, Fubini B, Ishimine Y, Tomatis M (2012) Sakurajima volcano: a physico-chemical study of the health consequences of long-term exposure to volcanic ash. Bull Volcanol 74:913–930. doi:10.1007/s00445-012-0575-3

Horwell CJ, Baxter PJ (2006) The respiratory health hazards of volcanic ash: a review for volcanic risk mitigation. Bull Volcanol 69:1–24. doi:10.1007/s00445-006-0052-y

Horwell CJ, Sparks RSJ, Brewer TS, Llewellin EW, Williamson BJ (2003) Characterization of respirable volcanic ash from the Soufrière Hills volcano, Montserrat, with implications for human health hazards. Bull Volcanol 65:346–362. doi:10.1007/s00445-002-0266-6

Horwell CJ, Le Blond JS, Michnowicz SAK, Cressey G (2010) Cristobalite in a rhyolitic lava dome: evolution of ash hazard. Bull Volcanol 72:249–253. doi:10.1007/s00445-009-0327-1

Horwell CJ, Williamson BJ, Donaldson K, Le Blond JS, Damby DE, Bowen L (2012) The structure of volcanic cristobalite in relation to its toxicity; relevance for the variable crystalline silica hazard. Particle Fibre Tech 9:44

Horwell CJ, Williamson BJ, Llewellin EW, Damby DE, Le Blond JS (2013) The nature and formation of cristobalite at the Soufrière Hills volcano, Montserrat: implications for the petrology and stability of silicic lava domes. Bull Volcanol 75:696. doi:10.1007/s00445-013-0696-3

Horwell CJ, Hillman SE, Cole PD, Loughlin SC, Llewellin EW, Damby DE, Christopher TE (2014) Controls on variations in cristobalite abundance in ash generated by the Soufrière Hills Volcano, Montserrat in the period 1997-2010. Geol Soc Lond Mem 39: 399–406. doi:10.1144/M39.21

Icenhower JP, Samson S, Lüttge A, McGrail BP (2004) Towards a consistent rate law: glass corrosion kinetics near saturation. Geol Soc London Spec Pub 236:579–594. doi:10.1144/GSL.SP.2004.236.01.32

Jay J, Costa F, Pritchard M, Lara LE, Singer BS, Herrin J (2014) Locating magma reservoirs using InSAR and petrology before and during the 2011-2012 Cordón Caulle silicic eruption. Earth Planet Sci Lett 395: 254–266. doi:10.1016/j.epsl.2014.03.046

Jones MT, Gislason SR (2008) Rapid release of metal salts and nutrients following the deposition of volcanic ash into aqueous environments. Geochim Cosmochim Acta 72:3661–3680. doi:10.1016/j.gca.2008.05.030

Jones JB, Segnit ER (1972) Genesis of cristobalite and tridymite at low temperatures. J Geol Soc Aust 18:419–422. doi:10.1080/00167617208728780

Kendrick JE, Lavallée Y, Hess K-U, De Angelis S, Ferk A, Gaunt HE, Meredith PG, Dingwell DB, Leonhardt R (2014) Seismogenic frictional melting in the magmatic column. Solid Earth 5:199–208. doi:10.5194/se-5-199-2014

Kingma KJ, Hemley RJ (1994) Raman spectroscopic study of microcrystalline silica. Am Mineral 79:269–273

Lange RA, Carmichael ISE (1990) Thermodynamic properties of silicate liquids with an emphasis on density, thermal expansion and compressibility. Rev Mineral 24:25–64

Lara LE, Naranjo JA, Moreno H (2004) Rhyodacitic fissure eruption in Southern Andes (Cordón Caulle; 40.5°S) after the 1960 (Mw: 9.5) Chilean earthquake: A structural interpretation. J Volcanol Geotherm Res 138:127–138

Lara LE, Moreno H, Naranjo JA, Matthews S, Pérez de Arce C (2006) Magmatic evolution of the Puyehue-Cordón Caulle Volcanic Complex (40° S), Southern Andean Volcanic Zone: From shield to unusual rhyolite fissure volcanism. J Volcanol Geotherm Res 157: 343–366

Le Blond JS, Cressey G, Horwell CJ, Williamson BJ (2009) A rapid method for quantifying single mineral phases in heterogeneous natural dusts using X-ray diffraction. Powder Diffract 24:17–23

Le Guern F, Bernard A (1982) A new method for sampling and analyzing volcanic sublimates - Application to Merapi Volcano, Java. J Volcanol Geotherm Res 12:133–146

Limaye A (2012) Drishti: a volume exploration and presentation tool. Depvelopments in X-Ray Tomography 85060X. doi:10.1117/12.935640

Lofgren G (1970) Experimental devitrification rate of rhyolite glass. Geol Soc Am Bull 81:553–560

Lofgren G (1971a) Experimentally produced devitrification textures in natural rhyolitic glass. Geol Soc Am Bull 82:111–124

Lofgren GE (1971b) Experimentally produced devitrification textures in natural rhyloitic glass. Geol Soc Am Bull 82:111–124

Martel C, Bourdier J-L, Pichavant M, Traineau H (2000) Textures, water content and degassing of silicic andesites from recent plinian and dome-forming eruptions at Mount Pelée volcano (Martinique, Lesser Antilles arc). J Volcanol Geotherm Res 96:191–206

Militzer AS (2013) The P-T-x evolution of the 2011-12 explosively and effusively erupted rhyolites at Puyehue-Cordón Caulle, Chile. Diplomarbeit zum Thema thesis. Unviersity of Mainz, Mainz, p 100

Mosesman MA, Pitzer KS (1941) Thermodynamic properties of the crystalline forms of silica. J Am Chem Soc 63:2348–2356. doi:10.1021/ja01854a013

Mossman BT, Glenn RE (2013) Bioreactivity of the crystalline silica polymorphs, quartz and cristobalite, and implications for occupational exposure limits (OELs). Crit Rev Toxicol 43:1–29. doi:10.3109/10408444.2013.818617

Mueller S, Melnik O, Spieler O, Scheu B, Dingwell DB (2005) Permeability and degassing of dome lavas undergoing rapid decompression: An experimental determination. Bull Volcanol 67:526–538. doi:10.1007/s00445-004-0392-4

Murphy MD, Sparks RSJ, Barclay J, Carroll MR, Brewer TS (2000) Remobilization of andesite magma by intrusion of mafic magma at the Soufriere Hills Volcano, Montserrat, West Indies. J Petrol 41:21–42

Mysen B, Richet P (2005) Silicate Glasses and Melts: Properties and Structure. Elsevier, Amsterdam, p 560

Nakada S, Motomura Y (1999) Petrology of the 1991-1995 eruption at Unzen: effusion pulsation and groundmass crystallization. J Volcanol Geotherm Res 89:173–196

Oelkers EH (2001) General kinetic description of multioxide silicate mineral and glass dissolution. Geochim Cosmochim Acta 65: 3703–3719

Okumura S, Nakamura M, Tsuchiyama A, Nakano T, Uesugi K (2008) Evolution of bubble microstructure in sheared rhyolite: Formation of a channel-like bubble network. J Geophys Res 113(B07208). doi:10.1029/2007JB005362

Okumura S, Nakamura M, Takeuchi S, Tsuchiyama A, Nakano T, Uesugi K (2009) Magma deformation may induce non-explosive volcanism via degassing through bubble networks. Earth Planet Sci Lett 281: 267–274. doi:10.1016/j.epsl.2009.02.036

Oxburgh R, Drever JI, Sun Y-T (1994) Mechanism of plagioclase dissolution in acid solution at 25 oC. Geochim Cosmochim Acta 58:661–669

Pallister JS, Thornber CR, Cashman KV, Clynne MA, Lowers HA, Mandeville CW, Brownfield IK, Meeker GP (2008) Petrology of the 2004-2006 Mount St. Helens lava dome - Implications for magmatic plumbing and eruption triggering. In: Sherrod DR, Scott WE, Stauffer PH (eds) A volcano rekindled: the renewed eruption of Mount St. Helens, 2004-2006. US Geological Survey Professional Paper. pp 647-702

Patrick MR, Dehn J, Dean K (2004) Numerical modeling of lava flow cooling applied to the 1997 Okmok eruption: Approach and analysis. J Geophys Res 109:B03202. doi:10.1029/2003JB002537

Pistolesi M, Cioni R, Bonadonna C, Elissondo M, Baumann V, Bertagnini A, Chiari L, Gonzales R, Rosi M, RFrancalanci L (2015) Complex dynamics of small-moderate volcanic events: the example of the 2011-12 rhyolitic Cordón Caulle eruption, Chile. Bull Volcanol 77:3. doi:10.1007/s00445-014-0898-3

Raga GB, Baumgardner D, Ulke AG, Torres Brizuela M, Kucienska B (2013) The environmental impact of the Puyehue–Cordon Caulle 2011 volcanic eruption on Buenos Aires. Nat Hazards Earth Syst Sci 13:2319–2330. doi:10.5194/nhess-13-2319-2013

Reich M, Zúñiga A, Amigo Á, Vargas G, Morata D, Palacios C, Parada MÁ, Garreaud RD (2009) Formation of cristobalite nanofibers during explosive volcanic eruptions. Geology 37:435–438. doi:10.1130/G25457A.1

Renders PJN, Gammons CH, Barnes HL (1995) Precipitation and dissolution rate constants for cristobalite from 150 to 300 oC. Geochim Cosmochim Acta 59:77–85. doi:10.1016/0016-7037(94)00232-B

Rosenberg PE (1988) Aluminum fluoride hydrates, volcanogenic salts from Mount Erebus, Antarctica. Am Mineral 73:855–860

Schipper CI, Castro JM, Tuffen H, James MR, How P (2013) Shallow vent architecture during hybrid explosive-effusive activity at Cordón Caulle (Chile, 2011-12): Evidence from direct observations and

pyroclast textures. J Volcanol Geotherm Res 262:25–37. doi:10.1016/j.jvolgeores.2013.06.005

Schneider CA, Rasband WS, Eliceiri KW (2012) NIH Image to ImageJ: 25 years of image analysis. Nat Methods 9:671–675

Shmulovich KI, Yardley BWD, Graham CM (2006) Solubility of quartz in crustal fluids: experiments and general equations for salt solutions and H2O-CO2 mixtures at 400-800 oC and 0.1-0.9 GPa. Geofluids 6:154–167. doi:10.1111/j.1468-8123.2006.00140.x

Silva Parejas C, Lara LE, Bertin D, Amigo A, Orozco G (2012) The 2011-2012 eruption of Cordón Caulle volcano (Southern Andes): Evolution, crisis management and current hazards. EGU General Assembly Abstracts 14(EGU2012-9382-2)

Singer BS, Jicha BR, Harper MA, Naranjo JA, Lara LE, Moreno-Roa H (2008) Eruptive history, geochronology, and magmatic evolution of the Puyehue-Cordón Caulle volcanic complex, Chile. Geol Soc Am Bull 120:599–618. doi:10.1130/B26276.1

Swanson SE, Naney MT, Westrich HR, Eichelberger JC (1989) Crystallization history of Obsidian Dome, Inyo Domes, California. Bull Volcanol 51:161–176

Talvitie NH (1964) Determination of free silica: Gravimetric and spectrophotometric procedures applicable to airborne settled dust. Am Ind Hyg Assoc J 25:169–178

Tuffen H, James MR, Castro JM, Schipper CI (2013) Exceptional mobility of an advancing rhyolitic obsidian flow at Cordón Caulle volcano in Chile. Nat Commun 4:2709. doi:10.1038/ncomms3709

Verma DK, Johnson DM, Des Tombe K (2002) A method for determining crystalline silica in bulk samples by Fourier transform infrared spectrophotometry. Ann Occup Hyg 46:609–615. doi:10.1093/annhyg/mef077

Vernier J-P, Fairlie TD, Murray JJ, Tupper A, Trepte C, Winker D, Pelon J, Garnier A, Jumelet J, Pavolonis M, Momar AH, Powell KA (2013) An Advanced System to Monitor the 3D Structure of Diffuse Volcanic Ash Clouds. J Appl Meteorol Climatol 52:2125–2138. doi:10.1175/JAMC-D-12-0279.1

Watkins J, Manga M, Huber C, Martin MC (2009) Diffusion-controlled spherulite growth in obsidian inferred from H2O concentration profiles. Contrib Mineral Petrol 157:163–172

Wilson T, Stewart C, Bickerton H, Baxter PJ, Outes V, Villarosa G, Rovere E (2013) Impacts of the June 2011 Puyehue-Cordón Caulle volcanic complex eruption on urban infrastructure, agriculture and public health. p 98

Wolff-Boenisch D, Gislarson SR, Oelkers EH (2004a) The effect of fluoride on the dissolution rates of natural glasses at pH 4 and 25 °C. Geochim Cosmochim Acta 68:4571–4582. doi:10.1016/j.gca.2004.05.026

Wolff-Boenisch D, Gislason SR, Oelkers EH, Putnis CV (2004b) The dissolution rates of natural glasses as a function of their composition at pH 4 and 10.6, and temperatures from 25 to 74 °C. Geochim Cosmochim Acta 68:4843–4858. doi:10.1016/j.gca.2004.05.027

Wright HMN, Weinberg RF (2009) Strain localization in vesicular magma: Implications for rheology and fragmentation. Geology 37:1023–1026. doi:10.1130/G30199A.1

Zhang Y (2008) Geochemical Kinetics. Princeton University Press, p 631